communications earth & environment

A Nature Portfolio journal

Article

https://doi.org/10.1038/s43247-025-02868-z

Impact-generated magnetite in Chang'e-5 soil as a potential recorder of lunar magnetism

Jinhua Li[1,2] ✉, Chaoqun Zhang[2,3], Chen Li[4], Yi Chen[2,5], Qinghua Zhang[6], Qianqian Lan[7], Yuqin Wang[1,2], Weiwei Wu[1,2], Jian Wang[8], Zheng Gong[9], Xu Tang[1], Xuechao Sha[10], Lixin Gu[1], Shiqi Cheng[1,2], Peiyu Liu[1,2], Jiawei Liu[2,3], Qiuli Li[2,5], Lin Gu[11], Gang Li[12], Yang Li[2,4], Rafal E. Dunin-Borkowski[7], Andrew P. Roberts[13] & Yongxin Pan[2,3]

Magnetite is a principal paleomagnetic recorder on Earth, but lunar magnetism is thought to be dominated by metallic iron and Fe-Ni alloys, with magnetite rare and typically sub-micrometer within troilite. We identify nanometer- to micrometer-scale magnetite in pentlandite-troilite assemblages from a Chang'e-5 regolith breccia. Magnetite occurs at and within pentlandite, locally enclosing pentlandite nanoinclusions, implying a formation pathway distinct from troilite-hosted occurrences. Textures and compositions indicate sequential crystallization from an impact-generated Fe-Ni-S-O melt: rapid pentlandite growth along troilite margins followed by magnetite nucleation at sulfide-silicate interfaces. The lunar low oxygen fugacity stabilizes Fe^{2+}-enriched magnetite, unlike terrestrial analogues. High crystallinity and single-domain to single-vortex states indicate strong remanence stability, making these grains reliable recorders of the contemporaneous lunar magnetic fields. These results broaden the inventory of lunar magnetic carriers, demonstrate impact-driven magnetite formation under lunar redox conditions, and motivate use of magnetite to refine the Moon's magnetic history.

Ferromagnetic minerals in planetary materials preserve unique archives of the origin, evolution, and intensity of planetary magnetic fields[1]. Among these minerals, magnetite (Fe_3O_4), a mixed-valence Fe^{2+}-Fe^{3+} oxide, plays a critical role on Earth[2], where its mineralogical and magnetic signatures underpin reconstructions of paleomagnetic fields[3,4], environmental and climate changes[5], and redox conditions controlled by temperature, pressure, oxygen, or sulfur fugacity[6,7]. Magnetite also records biological processes in diverse terrestrial settings[8].

By contrast, the lunar surface is airless, anhydrous, and markedly reduced, characterized by mantle oxygen fugacities several log units below the iron–wüstite (IW) buffer[9–14]. Such conditions are generally unfavorable for generating and preserving Fe^{3+}-bearing phases[7], underpinning the prevailing view that lunar magnetic carriers predominantly comprise metallic Fe and Fe-Ni alloys[15–18]. Nevertheless, indirect evidence for lunar magnetite has accumulated since the Apollo era through bulk rock-magnetic, electron-spin-resonance, and Mössbauer analyses[19–22]. Sub-micrometer magnetite was first unambiguously identified in Apollo 16 regolith breccia 60016[23] and more recently in Chang'e 5 (CE5) and Chang'e 6 (CE) lunar soils and glasses[24–26].

Despite these advancements, the physical, chemical, and magnetic properties of lunar magnetite remain poorly constrained. Formation mechanisms, variously attributed to oxidation of Fe metal, desulphurization of troilite in the presence of volatiles[23], or eutectoid crystallization from FeO-rich metals[24,25], are still debated. Its capacity to retain primary or secondary remanent magnetization is largely unexplored. Accordingly, metallic iron and Fe-Ni alloys are widely regarded as the principal carriers of lunar remanence[15–18,27].

Here, we document nanometer- to micrometer-scale magnetite crystals hosted within a pentlandite-troilite assemblage from CE5 regolith breccia sample CE5-023_P13. Using correlative atomic-scale structural, chemical, and magnetic analyses, we elucidate the nanostructure, composition, and magnetic domain states of these grains. These findings expand the known inventory of lunar magnetic carriers, offer additional insights into impact-melt processes, lunar redox conditions, and the preservation of remanent magnetization. This work thus provides fresh perspectives on lunar magnetic history and near-surface environmental evolution.

A full list of affiliations appears at the end of the paper. ✉e-mail: lijinhua@mail.iggcas.ac.cn

Results

Overview of the pentlandite-troilite assemblage in CE5 regolith breccia CE5-023_P13

To identify potential magnetic carriers in CE5 soils, we performed detailed scanning micro X-ray fluorescence (μXRF) analyses on Fe-Ni-rich particles in CE5-023 sample array[28]. Elemental mapping revealed several grains with distinct, spatially correlated Fe, Ni, and S enrichments (Supplementary Fig. 1a). Particle CE5-023_P13 was selected for comprehensive analysis due to its well-defined and co-localized Fe-Ni-S element signatures (Fig. 1a and Supplementary Fig. 1).

Using correlated three-dimensional X-ray microscopy (3D-XRM) and focused ion beam scanning electron microscopy (FIB-SEM)[28], we precisely located the Fe-Ni-S-bearing assemblage within the CE5-023_P13 particle and exposed it by serial FIB-SEM sectioning (Fig. 1b–g and Supplementary Movie 1). Subsequent 3D-XRM visualization combined with SEM cross-sectional imaging provided complementary insights into the particle's structural and compositional details (Supplementary Figs. 2–7).

Particle CE5-023_P13 is classified as an impact-melt breccia dominated by a feldspathic silicate matrix that hosts minor ilmenite, spinel, olivine, and sulfide phases (Fig. 1h–k, Supplementary Figs. 2–7 and Supplementary Movie 2). Micron- to submicron-scale vesicular glass along the particle rim (Fig. 1h, k) attest to rapid quenching shortly after emplacement. Within the matrix we distinguish (i) angular plagioclase clasts entrained from precursor lithologies, (ii) interstitial plagioclase microlites crystallized directly from the feldspathic melt, and (iii) subordinate mafic glass or microcrystalline domains (Fig. 1h–j). Together, these textures record partial crystallization of a transient impact-generated melt and the subsequent incorporation of diverse lithic and mineral fragments during brecciation[29].

Distinctively, sulfide minerals occur primarily as surface coating and penetrate as veinlets up to approximately 100 μm into the clast interior

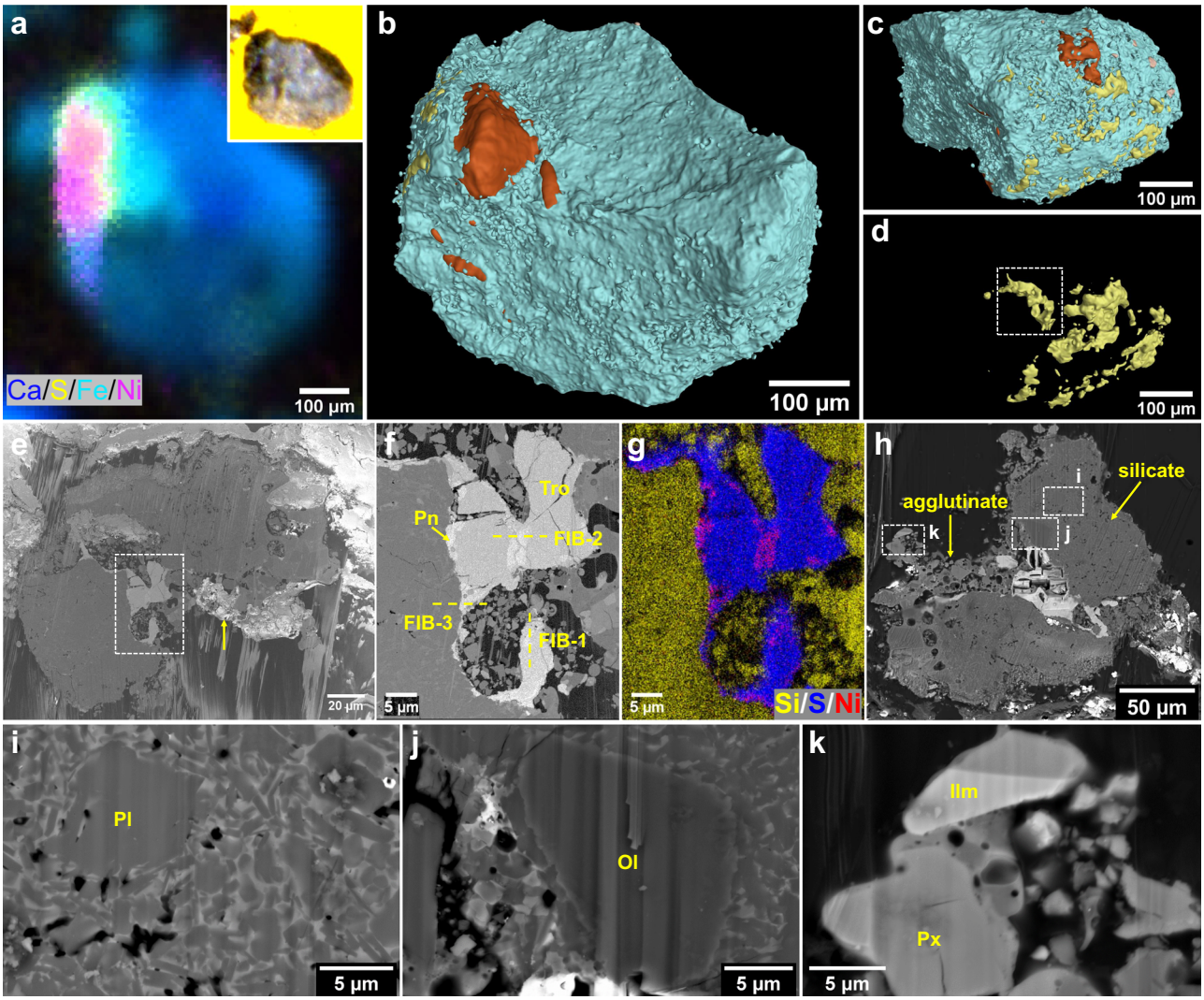

Fig. 1 | Identification of troilite-pentlandite assemblage in CE5-023_P13 by correlative μXRF, 3D-XRM, and FIB-SEM. a Combined element map acquired by scanning Micro X-ray fluorescence (μXRF) on the intact particle (Ca = blue, S = yellow, Fe = cyan, Ni = pink). Inset: stereomicroscopic image of CE5-023_P13. Three-dimensional X-ray microscopy (3D-XRM) renderings: **b** view matching the μXRF orientation; **c** orientation of the focused ion beam (FIB) milling plane; **d** highlighting of the sulfide-rich domain selected for detailed study (white dashed box). Colors: silicates = cyan, spinel = orange, sulfide = yellow. **e** Backscattered-electron scanning electron microscopy (BSE-SEM) image of the FIB-milled trench wall exposing the troilite-pentlandite assemblage (white dashed box). The high-reflectance areas (marked by yellow arrow) are residual silver paint applied to bridge the sample-stub gap and improve charge dissipation during SEM imaging. **f** Enlarged BSE-SEM image highlighting troilite (Tro) and pentlandite (Pn) contrasts. Yellow dashed lines mark sites of ultrathin lamellae extracted by FIB milling for transmission electron microscopy (TEM). **g** SEM-based energy dispersive X-ray spectroscopy (EDXS) elemental maps of the troilite-pentlandite assemblage (Si = yellow, S = blue, Ni = red). **h** BSE-SEM image of the polished cross-section after FIB skimming, with dashed boxes locating (**i**–**k**). Enlarged BSE-SEM images highlighting: **i** euhedral plagioclase (Pl) microcrystal, **j** olivine (Ol) microcrystal, and **k** vesiculated agglutinate hosting ilmenite (Ilm) and pyroxene (Px) microcrystals. Supplementary Figs. 1–7 and Supplementary Movies 1, 2 provide additional elemental, structural, and mineralogical information.

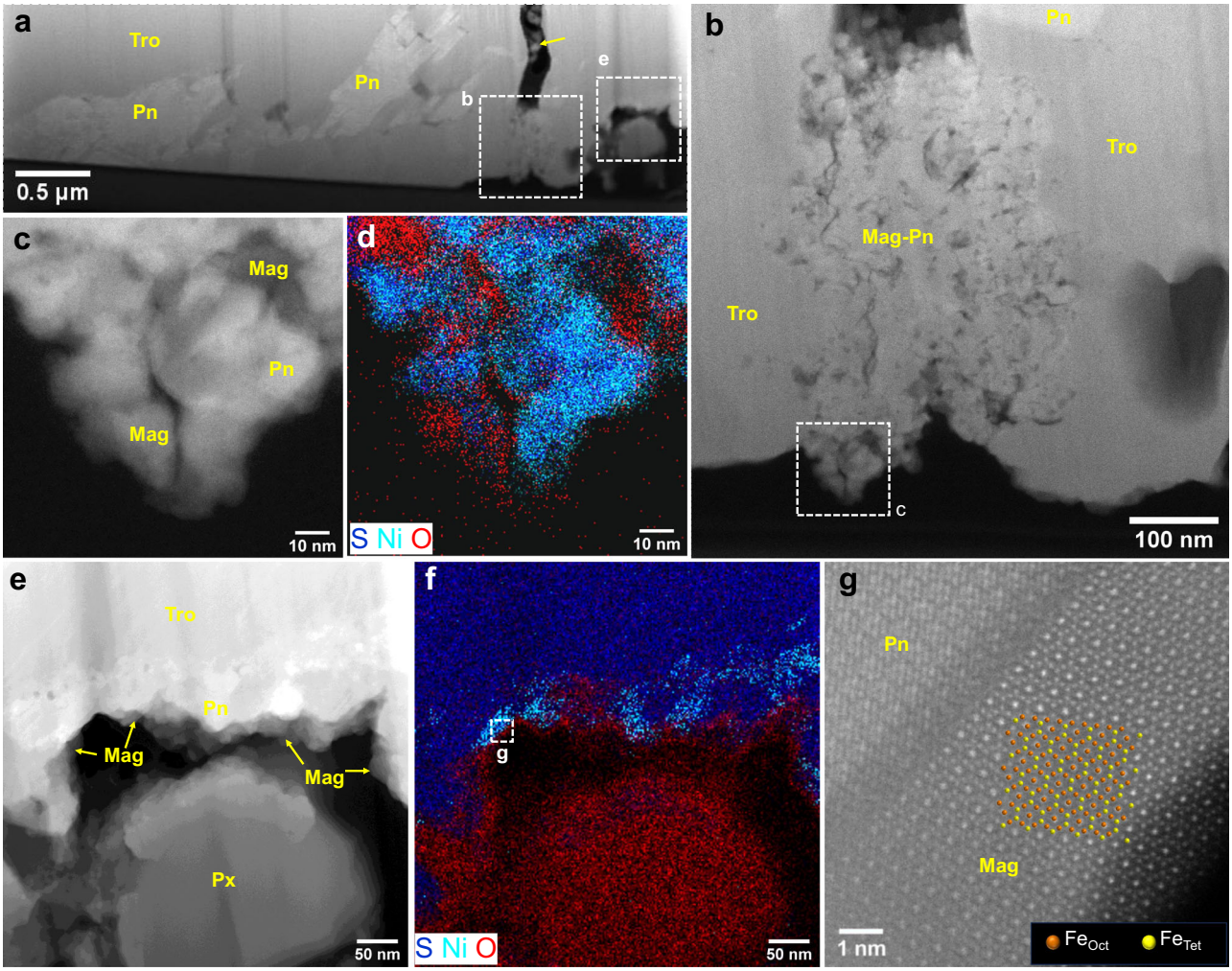

Fig. 2 | Identification of magnetite in the FIB-1 ultrathin section from particle CE5-023_P13. a Low-magnification HAADF-STEM image showing pentlandite (Pn) either enclosed in, or positioned along the edge of, a troilite (Tro) matrix. Microcrack (yellow arrow) partially filled by magnetite–pentlandite assemblages is highlighted by the dashed white box. **b** Enlarged HAADF-STEM overview of the boxed area in (**a**), illustrating nanometer- to submicron-scale magnetite (Mag) grains embedded in, or lining, pentlandite within troilite. **c** Further magnification of the region outlined in (**b**), emphasizing the spatial distribution of magnetite relative to pentlandite. **d** Corresponding STEM-EDXS elemental map (color overlay) for the area in (**c**) (S = blue, Ni = cyan, O = red), delineating the co-existence of magnetite and pentlandite. **e** HAADF-STEM image of a second sub-region (location in (**a**)) showing nanoscale magnetite decorating pentlandite grain boundaries and microcracks. Px pyroxene. **f** Corresponding STEM-EDXS elemental map (color overlay) for the area in (**e**) (S = blue, Ni = cyan, O = red). **g** Atomic-resolution HAADF-STEM image of the pentlandite-magnetite interface (white dashed box in (**f**)). Only Fe columns at octahedral (Oct) and tetrahedral (Tet) sites are resolved; a [1$\bar{1}$0] magnetite structure model is superimposed for reference. Supplementary Figs. 11–15 provide additional elemental, structural, and mineralogical information.

(Supplementary Fig. 2 and Supplementary Movie 2). The margins of these sulfide bodies display a micron-scale Fe-Ni-S rim, producing a pronounced concentric zonation (Fig. 1f, g and Supplementary Fig. 3).

Overall, the 3D-XRM and SEM data reveal a polyphase clast in which plagioclase microcrystals and minor mafic domains are cemented by iron-sulfide fragments, with accessory olivine, ilmenite and pyroxene microcrystals (Fig. 1h–k and Supplementary Figs. 3–7). The mineralogical textures record: (i) entrainment of a sulfide-rich melt into the feldspathic impact-melt breccia; (ii) rapid quenching that produced vesiculated agglutinates along the rim; and (iii) subsequent sub-solidus re-equilibration that generated the concentric Fe–Ni–S zoning.

Discovery and characterization of magnetite in the pentlandite-troilite assemblage

FIB-SEM milling was performed on the Fe-Ni-S-rich microregions, producing cross-sectional lamellae (~1 µm thick), which were subsequently thinned to ~100 nm for high-resolution transmission studies. Unexpectedly, these lamellae revealed micron- to nano-scale Fe-O-rich crystals closely associated with, or directly adjacent to, Fe-Ni-S domains (Supplementary Figs. 8–10). To minimize potential analytical artefacts due to repeated electron-beam exposure[30,31], three independent ultrathin sections were prepared separately for (i) mineralogical, (ii) chemical, and (iii) micromagnetic analyses (Fig. 1f).

High-angle annular dark-field scanning transmission electron microscopy (HAADF-STEM) imaging, combined with STEM-EDXS elemental mapping and atomic-resolution characterization of the FIB-1 section identified three chemically and structurally distinct phases (Fig. 2 and Supplementary Figs. 11–16): crystalline troilite (FeS), pentlandite ($(Fe,Ni)_9S_8$), and magnetite (Fe_3O_4). Notably, the troilite crystals lack vesicles, Si-bearing inclusions, or nanophase metallic Fe (Fig. 2a and Supplementary Figs. 11, 12), features typically indicative of space-weathered lunar sulfides[24,32]. The absence of these features suggests that the sulfide phases represent relatively pristine material. Textural relationships suggest emplacement of the sulfide melt droplet into a molten feldspathic highlands breccia, followed by entrapment during plagioclase crystallization.

Nanometer- to submicron-scale magnetite crystals preferentially nucleated along pentlandite grain boundaries. Magnetite–pentlandite assemblages are commonly found at the interface between troilite and the

surrounding silicate matrix: pentlandite lies in direct contact with troilite, whereas magnetite is positioned along the outer rim of pentlandite, facing either the silicate matrix or nearby micro-fractures. In some cases, magnetite and pentlandite occur together within the microcracks themselves (Fig. 2 and Supplementary Figs. 11–15). Fast Fourier transform (FFT) analysis of atomic-resolution images (Supplementary Fig. 15) yields crystallographic orientation relationships at phase boundaries. At the troilite-pentlandite interface, we identified the crystallographic relationships $[\bar{1}100]_{Tro}//[01\bar{1}]_{Pn}$ and $(0002)_{Tro}//(111)_{Pn}$, with closely matching lattice spacings $d(0002)_{Tro} \approx d(111)_{Pn}$, consistent with coherent exsolution textures[33]. Similarly, the magnetite-pentlandite interfaces exhibit a distinct orientation relationship of $(111)_{Pn}//(111)_{Mag}$ and $(1\bar{1}\bar{1})_{Pn}//(\bar{1}\bar{1}1)_{Mag}$, may suggest epitaxial nucleation and growth of magnetite on a structurally favorable pentlandite surface[34].

These atomic-scale insights, coupled with textural observations of the magnetite-pentlandite-troilite assemblage in the CE5-023_P13 regolith breccia, provide evidence for coherent exsolution of pentlandite from troilite, followed by nucleation and epitaxial growth of magnetite within and on pentlandite. This sequential crystallization, driven by late-stage cooling or mild post-impact oxidation, identifies magnetite an additional, potentially substantial ferromagnetic phase within lunar sulfide-bearing assemblages, complementing recent reports from other Chang'e samples and Apollo materials[23–26].

Crystal chemistry and microstructure of lunar magnetite

To better constrain the oxidation state and cation site occupancy of the CE5 magnetite, we analyzed the FIB-2 lamella (Fig. 3a) using synchrotron-based scanning transmission X-ray microscopy (STXM). This technique combines X-ray absorption spectroscopy (XAS) with X-ray magnetic circular dichroism (XMCD), providing element-, valence-, and site-specific characterization with a spatial resolution of ≤30 nm and an energy resolution of approximately 0.1 eV[35].

The Fe $L_{2,3}$-edge XAS spectrum for magnetite is shifted to higher energies relative to coexisting troilite, pentlandite, and olivine (Fig. 3b), indicating a comparatively higher mean Fe oxidation state. Consistent with their non-ferromagnetic properties[1], pentlandite and troilite exhibit negligible XMCD contrast (Supplementary Fig. 16). In contrast, magnetite displays pronounced dichroism (Fig. 3c). Its XMCD spectrum reveals a prominent Fe^{2+} signal at octahedral (O_h) sites, while signals corresponding to Fe^{3+} at both tetrahedral (T_d) and O_h sites are markedly subdued (Fig. 3d). This spectral signature distinctly differs from terrestrial magnetite, which typically exhibits clear $d^6Fe^{2+}O_h$, $d^5Fe^{3+}T_d$, and $d^5Fe^{3+}O_h$ components[36–38]. This observed XMCD signature thus implies either an excess of Fe^{2+}, a deficiency of Fe^{3+}, or a combination of both, in lunar magnetite.

Atomic-resolution HAADF-STEM imaging of the same magnetite crystal (Fig. 3e–k and Supplementary Fig. 17) shows direct contact with pentlandite on one side and the silicate matrix on the other. Internally, two distinct microstructural domains are present: (i) a predominant magnetite host characterized by structural coherence, and (ii) darker, low-contrast subdomains preserving the spinel lattice but exhibiting subtle crystallographic misorientations and reduced Fe/O atomic ratios (Fig. 3e–h). STEM-EDXS quantification confirms an Fe/O atomic ratio consistently lower than the ideal 42.8:57.2 for stoichiometric magnetite (Fig. 3h and Supplementary Fig. 18), indicating Fe-site vacancies consistent with Fe^{3+} deficiency.

In addition, bright, high-contrast nanoinclusions (<20 nm), identified as pentlandite, occur predominantly along grain boundaries and microcracks within magnetite (Fig. 3i–k and Supplementary Fig. 19). These inclusions often exhibit elongated morphologies (Fig. 3i, j). Atomic-resolution HAADF-STEM images further reveal coherent interfaces between pentlandite and magnetite lattices, with Fe columns shared at the interface (Fig. 3k), suggesting an epitaxial growth process during late-stage exsolution or infiltration of an Fe-Ni-S-O melt.

Collectively, the STXM and atomic-resolution HAADF-STEM observations demonstrate that lunar magnetite within the CE5-023_P13 breccia is chemically and structurally distinct from terrestrial magnetite, exhibiting pronounced Fe^{2+} enrichment, Fe^{3+} deficiency, and abundant pentlandite nanoinclusions. These characteristics reflect crystallization under the Moon's strongly reducing, sulfur-rich conditions, followed by limited chemical and structural re-equilibration during subsequent cooling.

Micromagnetic properties of lunar magnetite

Due to the embedding of magnetite grains within pentlandite-troilite matrices, direct determination of their three-dimensional morphologies is challenging and relies on interpretations from two-dimensional cross-sections. SEM and TEM analyses across three lamellae reveal individual crystals range in size from a few nanometers up to approximately 3 μm and display equant, elongate, or irregular shapes. Using these 2D observations, we reconstructed representative particle geometries for finite-element micromagnetic modeling[39]. Simulations suggest the population of magnetite grains covers the full range of magnetic domain states, from superparamagnetic (SP), through stable single-domain (SD), single-vortex (SV), to multi-domain (MD) states (Supplementary Figs. 20–22).

To further validate these theoretical predictions, we analyzed an exceptionally well-preserved, teardrop-shaped magnetite crystal (~800 × 500 nm) from the FIB-3 section (Fig. 4 and Supplementary Fig. 23) using room-temperature off-axis electron holography under field-free Lorentz STEM conditions[40]. The reconstructed magnetic phase image (Fig. 4e) was converted into a contour map representing the projected in-plane magnetic induction (Fig. 4f). In this map, contour spacing corresponds to field intensity, while colors and arrows denote vector direction. The experimental data unambiguously reveal a stable SV remanent magnetization state, closely matching predictions from micromagnetic modeling for a particle of similar dimensions and morphology (Fig. 4g).

Combined micromagnetic simulations and electron holography observations thus confirm that CE5 magnetite grains, spanning the stable SD to SV size ranges, can reliably retain stable, microscopically resolvable remanent magnetizations[41,42]. This finding underscores the value of lunar magnetite as robust carriers for reconstructing and interpreting the Moon's magnetic history.

Discussion

Magnetite on the lunar surface has been a subject of debate since the Apollo era[23]. It was first unequivocally identified within Apollo 16 regolith breccia sample 60016 by integrating electron microprobe analysis, X-ray absorption near-edge spectroscopy, and synchrotron-based X-ray diffraction[23]. In that work, magnetite was found in a clast characterized by banded textures intergrown with disseminated troilite, minor plagioclase fragments, pore spaces, and lunar silicate clasts. Excluding terrestrial contamination, direct magmatic crystallization, or oxidation of metallic iron or wüstite, the authors proposed magnetite formation via troilite desulfurization reactions induced by volatile-rich lunar vapors ($FeS + H_2O/CO_2 \rightarrow Fe_3O_4 + H_2/CO$)[23]. Subsequent TEM studies on CE5 lunar samples identified submicroscopic magnetite coexisting with metallic iron particles within oxygen-bearing Fe-S droplets, attributing its formation to eutectoid decomposition reactions during impact-induced melting ($4FeO \rightarrow Fe_3O_4 + Fe$)[24,25]. These studies implied that impacts involving iron-sulfide droplets and ilmenite-rich glasses promote magnetite formation on the lunar surface[24,25].

In contrast to these earlier models, the magnetite-pentlandite-troilite assemblage identified in the CE5-023_P13 regolith breccia exhibits distinctive mineralogical and textural relationships. Terrestrial contamination or alteration of our samples is considered unlikely because: (i) the analyzed regions are protected interiors isolated from pre-analytical exposure; (ii) sample preparation via correlative 3D-XRM and FIB-SEM serial sectioning avoided fluid/atmospheric contamination; and (iii) strict analytical protocols (e.g., minimizing repeated measurements and multi-technique analyses) ensure reliable compositional and textural data. Notably, the magnetite documented here differs fundamentally from typical terrestrial magnetite in its broad nano- to micrometer-scale grain-size/morphology

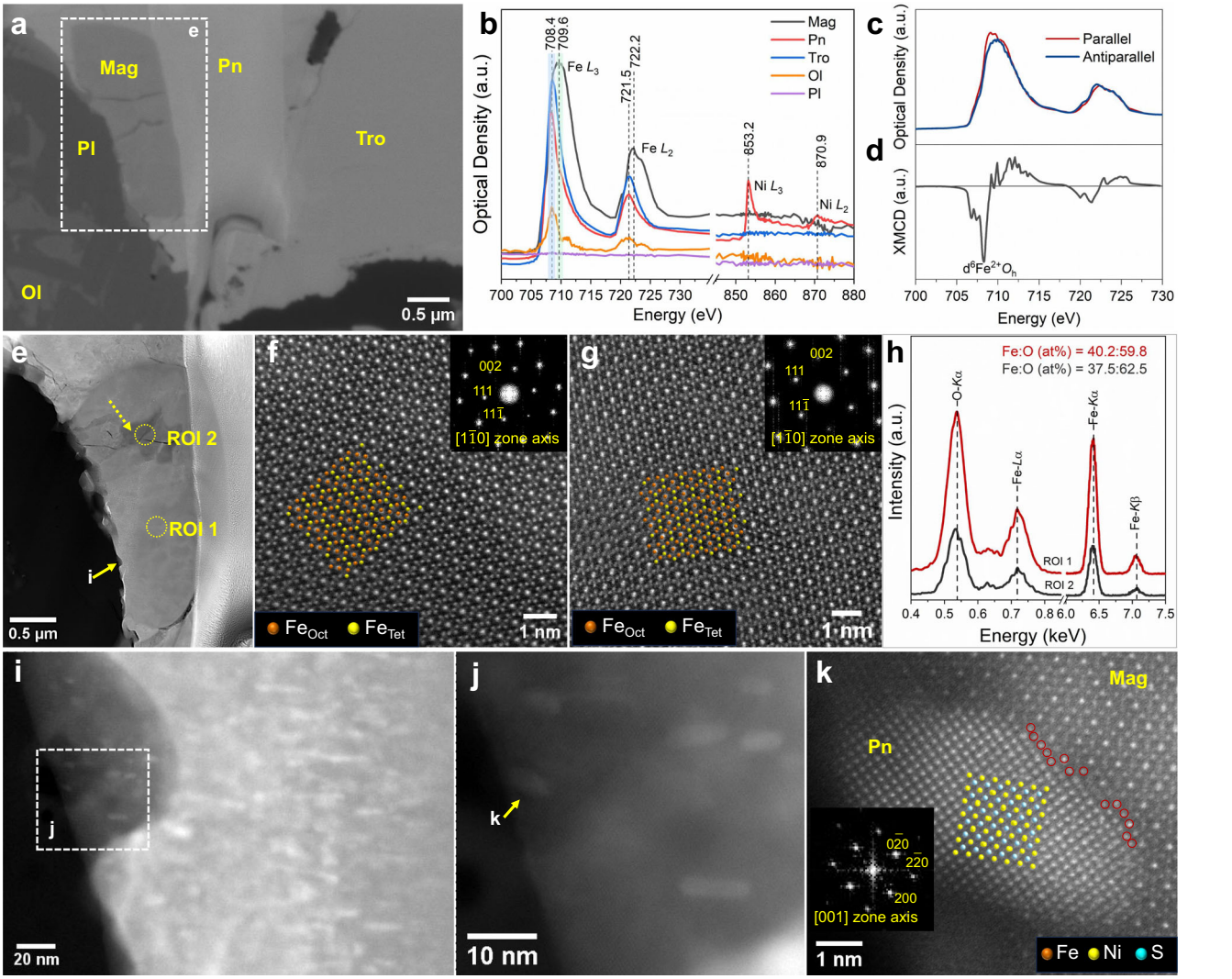

Fig. 3 | Chemical and structural characterization of magnetite in FIB-2 ultrathin section from particle CE5-023_P13. a BSE-SEM image of the ~1 μm-thick FIB lamella prior to final thinning (see Supplementary Fig. 9). Localized Ga implantation from FIB milling is visible in the upper pentlandite (Pent). **b** Fe $L_{2,3}$- and Ni $L_{2,3}$-edge XAS spectra for magnetite (Mag), pentlandite (Pn), troilite (Tro), plagioclase (Pl), and olivine (Ol). **c** Fe $L_{2,3}$-edge XAS spectra for magnetite with X-ray helicity parallel (μ^+) and antiparallel (μ^-) to a 0.6 T field. **d** Corresponding XMCD spectrum, dominated by Fe^{2+} at octahedral sites and showing subdued Fe^{3+} features. **e** Low-magnification HAADF-STEM image of a magnetite crystal flanked by pentlandite and plagioclase (white dashed box in (**a**)). Plagioclase in the lower-left corner is effectively invisible in the HAADF-STEM image because its low average atomic number produces negligible Z-contrast relative to the adjacent magnetite and pentlandite. A dark sub-domain (yellow dashed arrow) and bright nano-dots along the rim (yellow solid arrow) are highlighted. Atomic-resolution HAADF-STEM images from the dark micro-domain (**f**, ROI-2) and the host magnetite (**g**, ROI-1). Insets: FFT patterns with the [1$\bar{1}$0] spinel model superimposed; slight misorientations record twin boundaries. **h** Representative STEM-EDXS spectra from ROI-1 and ROI-2 microregions showing a lower Fe/O ratio in the darker relative to the host domain, Fe-richer region. **i** HAADF-STEM image of the magnetite rim (solid arrow in (**e**)) containing elongate pentlandite nanoinclusions. **j** Close-up of boxed area in **i**, illustrating the preferred orientation of pentlandite nanocrystals. **k** Atomic-resolution HAADF-STEM image of a pentlandite nanocrystal viewed down [001] zone axis (Fe atoms are not visualized along the [001] zone axis). Inset: FFT pattern and structural model. Red circles mark Fe atom columns shared across the coherent pentlandite-magnetite interface. Additional data and image series are provided in Supplementary Figs. 9, 16–19.

spectrum, pronounced Fe^{2+} enrichment, and abundant pentlandite nanoinclusions.

Both exogenous and endogenic pathways have been proposed for producing oxidized iron phases (e.g., magnetite) on the Moon. Exogenous delivery may occur via meteorites or hydrated impactors that introduce Fe^{3+}-bearing phases to the lunar surface[43]. Endogenic mechanisms include oxidation of ferrous or metallic iron, direct condensation from oxidizing gases vented by fumroles or degassing lava-flows, and direct crystallization from an already oxidized magmatic melt[44–47]. Based on textures and thermodynamic arguments for Apollo 16 regotith breccia 60016, Joy et al. (2015) proposed that magnetite formation by oxidization-driven replacement of Fe metal or desulphurization of troilite at <570 °C in the presence of H_2O/CO_2, with oxidants supplied by magmatic degassing or impact-released vapors[23]. By contrast, microanalyses of impact-processed troilite in CE5/CE6 samples identified widespread submicron magnetite with coexisting α-Fe and attributed this to eutectoid decomposition of FeO in Fe–S–O melts during impact heating, commonly accompanied by metallic Fe; oxygen-bearing volatiles generated during the impact may be critical[24–26].

Our observations differ in that pentlandite forms preferentially along troilite margins, whereas magnetite occurs adjacent to (or within) pentlandite and near the silicate matrix, rather than inside troilite. This geometry is difficult to reconcile with models that assume magnetite precipitates directly within troilite (desulfurization or FeO eutectoid) and instead points to a pentlandite-mediated, interface-controlled pathway during impact-melt colling. Magnetite's proximity to the silicate matrix rather than confinement within troilite strongly suggests that interactions at

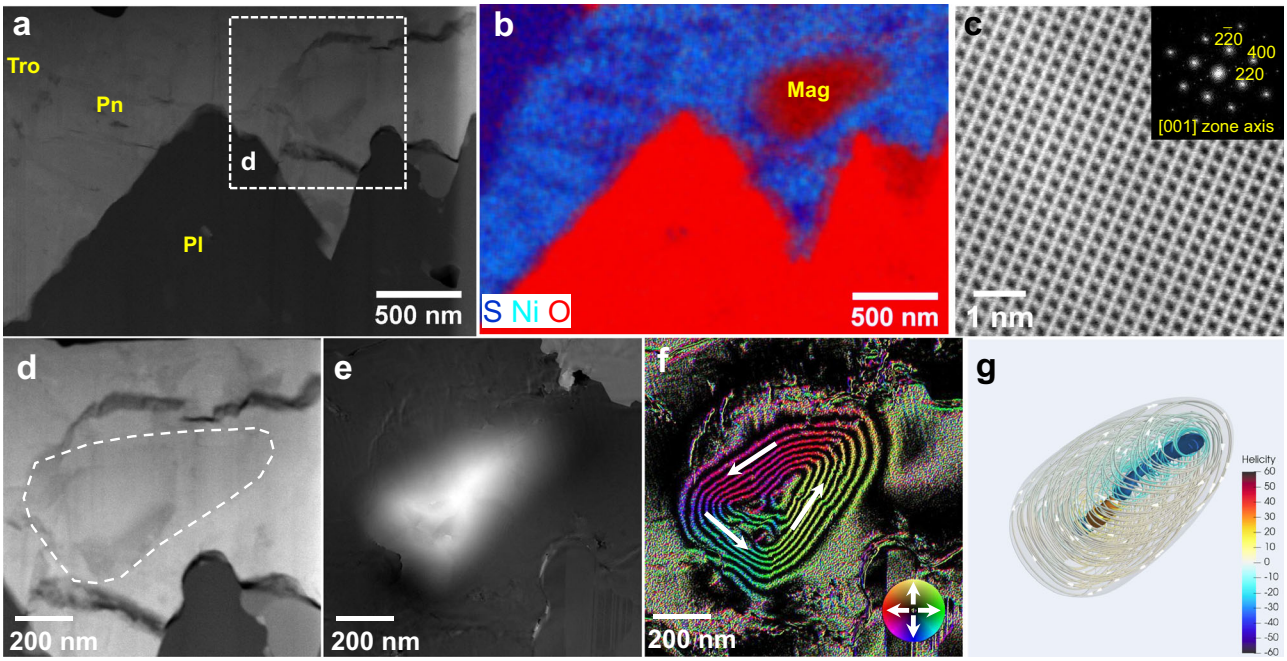

Fig. 4 | Magnetic microstructure of a lunar magnetite grain in FIB-3 ultrathin section from particle CE5-023_P13. a HAADF-STEM image showing a sub-micrometer magnetite (Mag) grain enclosed by pentlandite (Pn). Pl = plagioclase. Tro = troilite. **b** Corresponding STEM-EDXS elemental map (color overlay) showing a teardrop-shaped magnetite crystal (S = blue, Ni = cyan, O = red). **c** Atomic-resolution HAADF-STEM image of the magnetite recorded from the [001] zone axis. **d** Mean inner potential (MIP) phase image of the magnetite (white dashed outline). **e** Magnetic-phase image obtained by off-axis electron holography at room temperature, after subtraction of the MIP contribution. **f** Magnetic-phase contours (two times amplification; π rad spacing) reveal a single-vortex remanent state. Contour density reflects field strength; color wheel and arrows indicate in-plane induction orientation (white arrows shows representative directions). **g** Finite-element micromagnetic simulation for the same geometry reproduces the single-vortex structure; color scale denotes the induction magnitude.

sulfide–silicate interfaces, potentially mediated by pentlandite, control magnetite nucleation. This scenario contrasts with the homogeneous conditions envisioned in canonical Fe–S–O eutectoid models[24–26], underscoring the significance of pentlandite in directing magnetite formation and emphasizing the mineralogical context required to reconstruct lunar impact processes accurately. Taken together, the observed textures of magnetite, pentlandite, troilite, and surrounding glass are most consistent with sequential crystallization from an impact-generated Fe–Ni–S–O melt. In this model, pentlandite nucleates quickly along troilite margins, after which magnetite grows through reactions between pentlandite and the adjacent silicate melt. Verifying this scenario will require follow-up work, both on additional returned lunar soils and through dedicated laboratory experiments and numerical simulations that replicate impact-melt conditions. It should also be noted that, although magnetite has been reported in several lunar samples, apart from our pentlandite-associated case most occurrences are troilite-associated/hosted[23–26]. This pattern points to sulfide-mediated nucleation during specific impact-melt histories, but the overall abundance and distribution of lunar magnetite remain uncertain. Because troilite and lunar glass are labile and susceptible to beam/laser-induced oxidation during SEM/TEM/Raman (potentially creating Fe^{3+} phases and magnetite artefacts)[30,31], rigorously controlled, multi-technique surveys are needed. Priorities include unbiased searches in ilmenite- and silicate-rich domains, dose-calibrated microscopy, and isotopic/trace-element fingerprinting to verify in situ formation and to establish the properties required to use magnetite remanence reliably in lunar evolution studies.

SEM and TEM analyses show that lunar magnetite crystals exhibit ellipsoidal or irregular shapes with sizes spanning from nanometers to micrometers. Although full three-dimensional and crystallochemical characterization remains challenging, estimations based on terrestrial magnetite analogs suggest that grains smaller than ~30 nm likely exhibit SP behavior, contributing to magnetic susceptibility but not stable remanence[48]. Conversely, larger crystals (>30 nm) have the potential to carry robust thermoremanent magnetization (TRM) or thermochemical remanent magnetization (TCRM)[1,18,48]. Our TEM-based micromagnetic analyses confirm stable SD and SV states for these magnetite crystals, reinforcing their potential as stable magnetic carriers capable of preserving magnetization on billion-year timescales[49,50]. Consequently, lunar magnetite is likely an important contributor to crustal magnetic anomalies.

The origin, strength, and persistence of the Moon's magnetic field remain contentious. Global crustal anomalies and palaeomagnetic data imply a vigorous lunar dynamo active from >4.2 Ga to ~3.6 Ga, comparable in intensity to Earth's modern field[15,17], with intermittent weaker fields persisting up to ~0.9 Ga[51,52]. However, single-crystal paleointensity studies argue against a sustained core dynamo post-3.9 Ga, proposing impact-driven magnetic fields as the principal magnetizing mechanism for younger lunar samples[53–55]. The growing inventory of lunar magnetite[23–25], including pentlandite-hosted magnetite crystals reported here, points to impact processes as a major driver of magnetite formation across the lunar surface. Notably, the magnetite grains documented in this study (~30–3000 nm) occupy stable SD and SV size range and thus preserve remanent magnetization far more robustly than the smaller metallic iron and Fe-Ni alloy grains (~10–300 nm)[49,56]. Therefore, lunar magnetite constitutes an alternative target for rigorous paleointensity protocols such as Thellier-type experiments, potentially enabling more precise constraints on the timing, intensity, and spatial geometry of the lunar magnetic field and, by extension, deeper insights into the Moon's thermal and magnetic evolution.

Materials and methods

Sample preparation

The CE5 lunar soil analyzed in this study originated from a ~1 g scoop sample (CE5C0400YJFM00405) allocated by the China National Space Administration. Individual particles were initially screened for Fe-N-S enrichments using μXRF elemental imaging on the CE5-023 sample array. Particle CE5-023_P13 exhibited a particularly strong Ni signal and was selected for detailed analysis.

The particle was embedded in Buehler EpoxiCure™ 2, a hydrophobic, low-viscosity epoxy, within a 10 × 5 × 3 mm mold. Resin (part 20-3430) and Hardener (part 20-3432) were mixed at a 4:1 volume ratio, degassed under vacuum for 10 min, and cured overnight at room temperature in an anaerobic chamber. It was subsequently characterized at sub-micron resolution through non-destructive 3D-XRM. A region rich in Fe–Ni–S phases was identified and precisely located beneath the surface using a correlated 3D-XRM and FIB-SEM workflow[28]. Targeted Fe–Ni–S-rich lamellae (~1 μm thick) were extracted by FIB milling, followed by careful thinning to ~100 nm at 15 kV with decreasing current (maximum 700 pA), and final polishing at 2 kV and 10 pA to minimize beam damage to delicate Fe–O phases[57]. All ultrathin sections were protected under pure nitrogen during transfers and stored at −20 °C prior to analyses to prevent oxidation or contamination.

Micro XRF, 3D-XRM and SEM

Non-destructive μXRF elemental mapping experiments were performed using a Bruker M4 TORNADO PLUS μXRF spectrometer at the Institute of Geology and Geophysics, Chinese Academy of Sciences (IGG-CAS, Beijing). This instrument provides rapid, non-destructive elemental mapping with energy resolution <145 eV at Mn Kα and ~20 μm spatial resolution.

Correlative 3D XRM and FIB-SEM experiments on particle CE5-023_P13 were performed using a ZEISS Xradia 520 Versa X-ray microscope and a ZEISS Crossbeam 550 FIB-SEM with a gallium (Ga) ion source at the IGG-CAS (Beijing) and the ZEISS R&D Center (Shanghai). SEM imaging of carbon-coated FIB-polished sections was conducted at the IGG-CAS using a ZEISS Gemini 450 SEM equipped with an X-ray energy dispersive spectrometer and a pneumatically retractable BSE detector featuring a six-segment multimode solid-state sensor[58]. Integrated visualization and mineral segmentation based on 3D-XRM and FIB-SEM data were accomplished using ORS Dragonfly software v.2022.1.

TEM and synchrotron-based STXM

Ultrathin sections (~100 nm thickness) prepared by FIB milling were analyzed by TEM, HAADF-STEM and synchrotron-based STXM approaches. Conventional TEM experiments were using a JEOL JEM-2100 TEM instrument equipped with a LaB_6 electron gun, operating at 200 kV, and an Oxford X-Max EDXS detector. Atomic-resolution structural imaging and chemical characterization were carried out using a JEOL JEM-ARM200F microscope (Institute of Physics, Chinese Academy of Sciences, IP-CAS) and a ThermoScientific Spectra 300 microscope (ZEISS R&D Center, Shanghai). Both instruments are equipped with spherical aberration correctors, HAADF, and EDXS detectors for atomic-scale chemical and structural analyses.

Room-temperature off-axis electron holography measurements were performed at 300 kV in Lorentz mode using a Titan 80-300 TEM (Ernst Ruska-Center for Microscopy and Spectroscopy with Electrons, Forschungszentrum Jülich, Germany). Magnetic and mean inner potential phase components were separated by sample flipping, and holographic reconstructions were performed using Holowork 5.1 software.

Synchrotron-based STXM experiments were performed at the Canadian Light Source (CLS) 10ID-1 soft X-ray Spectromicroscopy (SM) Beamline[35]. Image stacks, which cover the 698-885 eV X-ray energy region for Fe *2p* and Ni *2p*, were recorded to analyze the local distribution and chemical state of Fe and Ni within ultra-thin sections. To determine the Fe $L_{2,3}$ XMCD, two STXM image stacks were obtained with both a left- (LCP, which is the parallel direction) and right- (RCP, antiparallel direction) circularly polarized X-ray beam. Both STXM-derived XAS and XMCD data analyses were performed with the aXis2000 software package[59].

Micromagnetic modeling

Room-temperature (293.15 K) micromagnetic simulations were performed using finite-element particle models constructed and meshed with Coreform Cubit 2024.3. Simulations were executed with the MERRILL code (version 1.8.6)[60]. Finite-element mesh sizes matched magnetite's exchange length (~3–9 nm) and scaled according to particle size. Visualization of simulation outputs was performed using ParaView 5.11.1.

Data availability

Source data are provided with this paper. All data generated in this study are provided in the Supplementary Data file and deposited in the Figshare repository (https://doi.org/10.6084/m9.figshare.30234484).

Received: 8 December 2024; Accepted: 2 October 2025;
Published online: 10 November 2025

References

1. Harrison, R. J. & Feinberg, J. M. Mineral magnetism: providing new insights into geoscience processes. *Elements* **5**, 209–215 (2009).
2. Maher, B. Ubiquitous magnetite. *Nat. Geosci.* **17**, 7–7 (2024).
3. Dunlop, D. J. Magnetic recording in rocks. *Phys. Today* **65**, 31–37 (2012).
4. Tarduno, J. A. et al. Paleomagnetism indicates that primary magnetite in zircon records a strong hadean geodynamo. *Proc. Natl. Acad. Sci. USA* **117**, 2309–2318 (2020).
5. Liu, Q. et al. Environmental magnetism: principles and applications. *Rev. Geophys*. **50**, RG4002 (2012).
6. Dare, S. A. S. et al. Trace elements in magnetite as petrogenetic indicators. *Miner. Deposita* **49**, 785–796 (2014).
7. Nadoll, P., Angerer, T., Mauk, J. L., French, D. & Walshe, J. The chemistry of hydrothermal magnetite: a review. *Ore Geol. Rev.* **61**, 1–32 (2014).
8. Pósfai, M. L. & Dunin-Borkowski, R. E. Magnetic nanocrystals in organisms. *Elements* **5**, 235–240 (2009).
9. Wadhwa, M. Redox conditions on small bodies, the moon and mars. *Rev. Mineral. Geochem.* **68**, 493–510 (2008).
10. Sato, M. The driving mechanism of lunar pyroclastic eruptions inferred from the oxygen fugacity behavior of Apollo 17 orange glass. In *Proc. 10th Lunar Planet. Sci. Conf.* Vol. 1, 311–325 (Pergamon Press, Inc., 1979).
11. Sato, M., Hickling, N. L. & McLane, J. E. Oxygen fugacity values of Apollo 12, 14, and 15 lunar samples and reduced state of lunar magmas. In *Proc. 4th Lunar Sci. Conf., Geochim. Cosmochim. Acta Suppl.* Vol. 4, 1061–1079 (Pergamon Press, Inc., 1973).
12. Zhang, H. et al. Long-term reduced lunar mantle revealed by Chang'e-5 basalt. *Nat. Commun.* **15**, 8328 (2024).
13. Longhi, J. Experimental petrology and petrogenesis of mare volcanics. *Geochim. Cosmochim. Acta* **56**, 2235–2251 (1992).
14. Haggerty, S. E. The redox state of planetary basalts. *Geophys. Res. Lett.* **5**, 443–446 (1978).
15. Wieczorek, M. A. et al. Lunar magnetism. *Rev. Mineral. Geochem.* **89**, 207–241 (2023).
16. Rochette, P., Gattacceca, J., Ivanov, A. V., Nazarov, M. A. & Bezaeva, N. S. Magnetic properties of lunar materials: meteorites, luna and apollo returned samples. *Earth Planet. Sci. Lett.* **292**, 383–391 (2010).
17. Weiss, B. P. & Tikoo, S. M. The lunar dynamo. *Science* **346**, 1246753 (2014).
18. Li, J. et al. Magnetic signatures and origins of ferromagnetic minerals in Chang'e-6 lunar farside soils. *Nat. Commun.* **16**, 6218 (2025).
19. Jedwab, J., Herbosch, A., Wollast, R., Naessens, G. & Van Geen-Peers, N. Search for magnetite in lunar rocks and fines. *Science* **167**, 618–619 (1970).
20. Griscom, D., Friebele, E. & Marquardt, C. Evidence for a ubiquitous, sub-microscopic "magnetite-like" constituent in the lunar soils. In *Proc. 4th Lunar Sci. Conf., Geochim. Cosmochim. Acta Suppl.* Vol. 4, 2709–2727 (Pergmon Press, Inc., 1973).
21. McSween, H. Y. A new type of chondritic meteorite found in lunar soil. *Earth Planet. Sci. Lett.* **31**, 193–199 (1976).

22. Zolensky, M. E., Weisberg, M. K., Buchanan, P. C. & Mittlefehldt, D. W. Mineralogy of carbonaceous chondrite clasts in HED achondrites and the moon. *Meteorit. Planet. Sci.* **31**, 518–537 (1996).
23. Joy, K. H. et al. Identification of magnetite in lunar regolith breccia 60016: evidence for oxidized conditions at the lunar surface. *Meteorit. Planet. Sci.* **50**, 1157–1172 (2015).
24. Guo, Z. et al. Sub-microscopic magnetite and metallic iron particles formed by eutectic reaction in Chang'E-5 lunar soil. *Nat. Commun.* **13**, 7177 (2022).
25. Cao, Z. et al. Submicroscopic magnetite may be ubiquitous in the lunar regolith of the high-Ti region. *Sci. Adv.* **10**, eadn2301 (2024).
26. Pang, R. et al. Impact-induced magnetite is widespread on the near and far sides of the moon. *Earth Planet. Sci. Lett.* **669**, 119572 (2025).
27. Tikoo, S. M. et al. A two-billion-year history for the lunar dynamo. *Sci. Adv.* **3**, e1700207 (2017).
28. Li, J. et al. Rapid screening of Zr-containing particles from Chang'e-5 lunar soil samples for isotope geochronology: technical roadmap for future study. *Geosci. Front.* **13**, 101367 (2022).
29. Shi, Y. et al. Petrological, chemical, and chronological study of breccias in the Chang'e-5 soil. *Meteorit. Planet. Sci.* **59**, 2296–2320 (2024).
30. Gu, L. et al. Measurement of ferric iron in chang'e-5 impact glass beads. *Earth Planets Space* **75**, 151 (2023).
31. Li, X. et al. Thermally induced phase transition of troilite during micro-raman spectroscopy analysis. *Icarus* **390**, 115299 (2023).
32. Gu, L. et al. Space weathering of the chang'e-5 lunar sample from a mid-high latitude region on the moon. *Geophys. Res. Lett.* **49**, e2022GL097875 (2022).
33. Tang, X. et al. Origin and implication of pentlandite in Chang'e-5 lunar soils. *Lithos* **458-459**, 107342 (2023).
34. Zheng, L., Hu, X., Kang, X. & Li, D. Precipitation of $M_{23}C_6$ and its effect on tensile properties of 0.3C–20Cr–11Mn–1Mo–0.35N steel. *Mater. Des.* **78**, 42–50 (2015).
35. Wang, J. & Li, J. Scanning transmission x-ray microscopy at the Canadian Light Source: progress and selected applications in geosciences. *At. Spectrosc.* **43**, 84–98 (2022).
36. Coker, V. S. et al. Cation site occupancy of biogenic magnetite compared to polygenic ferrite spinels determined by X-ray magnetic circular dichroism. *Eur. J. Mineral.* **19**, 707–716 (2007).
37. Henderson, C. M. B., Pearce, C. I., Charnock, J. M., Harrison, R. J. & Rosso, K. M. An x-ray magnetic circular dichroism (XMCD) study of Fe ordering in a synthetic $MgAl_2O_4$-Fe_3O_4 (spinel-magnetite) solid-solution series: implications for magnetic properties and cation site ordering. *Am. Mineral.* **101**, 1373–1388 (2016).
38. Li, J. et al. Controlled cobalt doping in the spinel structure of magnetosome magnetite: new evidences from element- and site-specific X-ray magnetic circular dichroism analyses. *J. R. Soc. Interface* **13**, 20160355 (2016).
39. Wang, Y., Ge, K., Liu, S. & Li, J. Micromagnetic modeling: technological advances and new applications in nanogeosciences (in Chinese). *Chin. Sci. Bull.* **70**, 1–22 (2025).
40. Dunin-Borkowski, R. E., McCartney, M. R., Smith, D. J. & Parkin, S. S. P. Towards quantitative electron holography of magnetic thin films using in situ magnetization reversal. *Ultramicroscopy* **74**, 61–73 (1998).
41. Nagy, L. et al. Stability of equidimensional pseudo–single-domain magnetite over billion-year timescales. *Proc. Natl. Acad. Sci. USA* **114**, 10356–10360 (2017).
42. Roberts, A. P. et al. Resolving the origin of pseudo-single domain magnetic behavior. *J. Geophys. Res.* **122**, 9534–9558 (2017).
43. Wasilewski, P. J. Shock remagnetization associated with meteorite impact at planetary surfaces. *The Moon* **6**, 264–291 (1973).
44. Williams, R. J. & Gibson, E. K. The origin and stability of lunar goethite, hematite and magnetite. *Earth Planet. Sci. Lett.* **17**, 84–88 (1972).
45. Dikov, Y. P., Gerasimov, M. V., Yakovlev, O. I. & Ivanov, A. V. Valence state of iron in a condensate from the Luna 16 regolith. *Petrology* **17**, 429–438 (2009).
46. Yakovlev, O. I., Dikov, Y. P. & Gerasimov, M. V. Effect of the disproportionation reaction of ferrous iron in impact-evaporation processes. *Geochem. Int.* **47**, 134–142 (2009).
47. Shearer, C. K. et al. Chlorine distribution and its isotopic composition in "rusty rock" 66095. Implications for volatile element enrichments of "rusty rock" and lunar soils, origin of "rusty" alteration, and volatile element behavior on the Moon. *Geochim. Cosmochim. Acta* **139**, 411–433 (2014).
48. Muxworthy, A. R. & Williams, W. Critical single-domain/multidomain grain sizes in noninteracting and interacting elongated magnetite particles: Implications for magnetosomes. *J. Geophys. Res.* **111**, B12S12 (2006).
49. Nagy, L., Williams, W., Tauxe, L. & Muxworthy, A. R. From nano to micro: evolution of magnetic domain structures in multidomain magnetite. *Geochem. Geophys. Geosyst.* **20**, 2907–2918 (2019).
50. Wang, Y. et al. Micromagnetic modeling of a magnetically unstable zone and its geological significances. *J. Geophys. Res.* **127**, e2022JB024876 (2022).
51. Mighani, S. et al. The end of the lunar dynamo. *Sci. Adv.* **6**, eaax0883 (2020).
52. Tikoo, S. M. & Evans, A. J. Dynamos in the inner solar system. *Annu. Rev. Earth Planet. Sci.* **50**, 99–122 (2022).
53. Tarduno, J. A. et al. Absence of a long-lived lunar paleomagnetosphere. *Sci. Adv.* **7**, eabi7647 (2021).
54. Cottrell, R. D., Zhou, T. & Tarduno, J. A. Dataset of replicate Apollo sample magnetizations bearing on impacts and absence of a long-lived lunar dynamo. *Sci. Data* **11**, 807 (2024).
55. Zhou, T. et al. A lunar core dynamo limited to the moon's first ~140 million years. *Commun. Earth Environ.* **5**, 456 (2024).
56. Muxworthy, A. R. & Williams, W. Critical single-domain grain sizes in elongated iron particles: implications for meteoritic and lunar magnetism. *Geophys. J. Int.* **202**, 578–583 (2015).
57. Bassim, N. D. et al. Minimizing damage during FIB sample preparation of soft materials. *J. Microsc.* **245**, 288–301 (2012).
58. Yuan, J. et al. Rapid recognition and quantitative analysis of niobium minerals by scanning electron microscopy/energy dispersive X-ray spectroscopy. *J. Anal. At. Spectrom.* **37**, 2392–2400 (2022).
59. Hitchcock, A. P. Analysis of X-ray images and spectra (aXis2000): a toolkit for the analysis of X-ray spectromicroscopy data. *J. Electron. Spectrosc. Relat. Phenom.* **266**, 147360 (2023).
60. Ó Conbhuí, P. et al. MERRILL: micromagnetic earth related robust interpreted language laboratory. *Geochem. Geophys. Geosyst.* **19**, 1080–1106 (2018).

Acknowledgements

We appreciate all staff of China's Chang'e Lunar Exploration Project for their dedication in returning lunar samples. This work was financially supported by the National Natural Science Foundation of China (Grants 42225402 and 42388101) and the Key Research Program of the Institute of Geology & Geophysics, CAS (Grants IGGCAS-202202 and ICCCAS-202401). We thank Jian Ding at Thermo Fisher Customer Center (Shanghai) for providing access to TEM facilities, and engineers Haifeng Gao and Suya Liu for their assistance with TEM experiments. Synchrotron STXM experiments (CLS Proposal 23-7537) were performed at the 10ID-1 SM beamline, Canadian Light Source, which is supported by the Natural Sciences and Engineering Research Council of Canada, the National Research Council of Canada, the Canadian Institutes of Health Research, the Province of Saskatchewan, Western Economic Diversification Canada, and the University of Saskatchewan.

Author contributions

JH.L., QL.L., L.G., and G.L. acquired the lunar soil samples. JH.L. and YX.P. conceived and designed the study. JH.L., CQ.Z., and XC.S. performed 3D XRM experiments. JH.L., CQ.Z., QH.Z., and WW.W. performed SEM and TEM experiments. QQ.L. and RE.DB. conducted electron holography experiments. J.W. performed synchrotron experiments. YQ.W. and JH.L. performed micromagnetic simulations. JH.L. CQ.Z., Y.C., X.T., LX.G., SQ.C., JW.L., C.L., Y.L., and PY.L. analyzed the data. JH.L. wrote the manuscript with input from Z.G., AP.R,. and Y.C. All authors contributed to discussions and manuscript review.

Competing interests

The authors declare no competing interests.

Additional information

Supplementary information The online version contains supplementary material available at https://doi.org/10.1038/s43247-025-02868-z.

Correspondence and requests for materials should be addressed to Jinhua Li.

Peer review information *Communications Earth & Environment* thanks Katherine Joy, Brittany Cymes, and the other anonymous reviewer(s) for their contribution to the peer review of this work. Primary handling editors: Joe Aslin. A peer review file is available.

[1]Key Laboratory of Deep Petroleum Intelligent Exploration and Development, Institute of Geology and Geophysics, Chinese Academy of Sciences, Beijing, China. [2]College of Earth and Planetary Sciences, University of Chinese Academy of Sciences, Beijing, China. [3]Key Laboratory of Earth's Deep Interior, Institute of Geology and Geophysics, Institute of Geology and Geophysics, Chinese Academy of Sciences, Beijing, China. [4]Center for Lunar and Planetary Sciences, Institute of Geochemistry, Chinese Academy of Sciences, Guiyang, China. [5]State Key Laboratory of Lithospheric and Environmental Coevolution, Institute of Geology and Geophysics, Chinese Academy of Sciences, Beijing, China. [6]Beijing National Laboratory for Condensed Matter Physics, Institute of Physics, Chinese Academy of Sciences, Beijing, China. [7]Ernst Ruska-Centre for Microscopy and Spectroscopy with Electrons, Peter Grünberg Institute, Forschungszentrum Jülich, Jülich, Germany. [8]Canadian Light Source Inc., University of Saskatchewan, Saskatoon, SK, Canada. [9]State Key Laboratory for Mineral Deposits Research, School of Earth Sciences and Engineering, Nanjing University, Nanjing, China. [10]ZEISS Microscopy Customer Center, Beijing, China. [11]Beijing National Center for Electron Microscopy and Laboratory of Advanced Materials, School of Materials Science and Engineering, Tsinghua University, Beijing, China. [12]Institute of High Energy Physics, Chinese Academy of Science, Beijing, China. [13]Research School of Earth Sciences, Australian National University, Canberra, ACT, Australia. ✉e-mail: lijinhua@mail.iggcas.ac.cn